

RESEARCH PAPER

Computational simulations of nanoparticle transport in a three-dimensional capillary network

Sadegh Shurche ^{1*}, Mohammad Yousefi Sooteh ²

¹Department of Physics and Medical Engineering, School of Medicine, Tehran University of Medical Sciences, Tehran, Iran

²Department of Medical Physics, School of Medicine, Tabriz University of Medical Sciences, Tabriz, Iran

ABSTRACT

Objective(s): Multifunctional nanomedicine is the new generation of medicine, which is remarkably promising and associated with the minimum toxicity of targeted therapy. Distribution and transport of nanoparticles (NPs) in the blood flow are essential to the evaluation of delivery efficacy.

Materials and Methods: In the present study, we initially designed a phantom based on Murray's minimum work law using the AutoCAD software. Afterwards, the phantom was fabricated using lithography and imaged using a Siemens Magnetom 3T Prisma MRI scanner at the National Brain Mapping Laboratory, Iran. Finally, the velocity and pressure in the capillary network were simulated using the COMSOL software. Moreover, three-dimensional Navier-Stokes equations were applied to model the NP transport and dispersion in blood suspension.

Results: According to the findings, particle size, vessel geometry, and vascular flow rate affected the delivery efficacy and NP distribution. Cerebral blood flow, cerebral blood volume, mean transit time, and curves for the capillary network were obtained at different times. The simulations indicated that the velocity and pressure in the capillary network were within the ranges of 0.0001-0.0005 m/s and 5-25 mm/Hg, respectively. Higher particle concentration was also observed in the non-uniform NP distribution profile near the vessel wall.

Conclusion: We investigated the effects of the vessel size and geometry and particulate nature of blood on the delivery and distribution of NPs. For targeted drug delivery applications, a mechanistic understanding on the nanomedicine design was provided as well.

Keywords: Capillary network, Finite element method, Nanoparticle, Simulation

How to cite this article

Shurche S, Yousefi Sooteh M. Computational simulations of nanoparticle transport in a three-dimensional capillary network. *Nanomed J.* 2019; 6(4): 291-300. DOI: 10.22038/nmj.2019.06.000007

INTRODUCTION

In recent years, several nanoplatforms have been proposed as image probing agents and smart drug carriers. Various studies have introduced new nanoplatforms, such as liposomes [1, 2], Au/Si/polymer shells, dendrimers, polymeric micelles [3], quantum dots[4], and nanoparticles [5]. Since nanoparticles (NPs) offer potential applications and unique characteristics, special attention has been paid to their wide range of applications by engineers, medical researchers, and scientists. For instance, in combating cardiovascular diseases, NPs have proven capable of imbibing drugs into their core or coating drugs to their surface.

* Corresponding Author Email: sadegh.shurche@yahoo.com

Note. This manuscript was submitted on June 7, 2019; approved on August 1, 2019

Advanced microfabrication technology is able to modulate the half-life of NPs through selective distribution, as well as circulation based on their size and shape. Some environmental parameters could trigger active and controlled drug release, such as light intensity, temperature, and pH level.

NP binding and distribution are strongly influenced by size, shape, and surface chemistry. For instance, the parameter of size has been extensively investigated in a review, and its major impact on NP binding and distribution has been confirmed. Moreover, organs such as the liver, spleen, and bone marrow could efficiently filter spherical particles with larger sizes than 200 nanometers. In contrast, particles with smaller sizes than 10 nanometers may be cleared fast through extravasation or by the kidneys. Therefore, the

optimum range for the size of circulating spherical carriers would be 10-200 nanometers.

Similarly, the parameter of shape is considered to be a fundamental feature in micro/nanoparticles. Due to their surface tension, most NPs have a spherical shape. However, several shapes of NPs have recently been developed. For instance, nanorods with desired aspect ratios are currently available for molecular imaging and photothermal cancer therapy [6]. Moreover, asymmetrically functionalized AuNPs have been introduced in [7], which could be used to fabricate nanochains [8]. In tumor targeting, super paramagnetic iron oxide-based nanowires have also been investigated [9], and covalent-bonding nano-necklaces have been developed using gold NPs [10].

There has been remarkable advancement in NPs compared to conventional drug carriers. Nevertheless, their binding, transport, and distribution are not thoroughly comprehended. One of the reasons for this uncertainty is the small size of NPs, which makes it difficult to visualize NPs *in-vivo* with the dimension range of 10 to a few hundred nanometers. The other reason is the complexity of the biological environment *in-vivo* for the NPs involving the blood flow, circulation, extravasation, and elimination. Since the liver is able to filter NPs, they could be removed by the spleen and attach to healthy cells; as such, they are not always able to reach the targeted site.

Some key factors must be considered in the attempt to obtain proper delivery efficacy, including size, the parameters of the diseased region, physical parameters of the patient, and location. Physical parameters of patients include the blood flow rate, vascular diameter, blood components, and surface area. The NP-targeted delivery in the vascular system involves a hydrodynamic force, the transport interaction, and multivalent interactions with the targeted biosurfaces. Since the size of NPs is small, the delivery procedure is dynamic, and the vascular environment is complex. Consequently, the experimental study of these phenomena is substantially challenging *in-vivo*. In this regard, a mathematical tool that is able to evaluate and predict the NP transport and distribution is required. To date, the theoretical studies regarding NP deposition on a micro scale have not stepped beyond the simple spherical particles, which have only been evaluated in the optimum condition in a two-dimensional channel affected by the shear flow [10].

Addition of different designs for the blood flow and complicated vascular condition makes it impossible to predict the behavior of particles. Models of continuum convection-diffusion-reaction on a macro scale have been extensively applied for the modeling of the drug delivery procedure. For instance, modeled the delivery of spherical NPs in a tumor. In the magnetic NPs in the vascular flow were examined using computational fluid dynamics, while in , the deposition of NPs in the respiratory tract was investigated. However, the continuum model is not capable of providing details on the effects of shape, size, shear dependency, and ligand-receptor density on NP binding. The present study aimed to model NP transport and distribution as influenced by the blood flow and complex vessel geometries.

MATERIALS AND METHODS

Theoretical basis

Most perfusion models consist of two basic models, including the Kety-Schmidt model [11] for the penetration of the contrast agents and Meier-Zierler model for the non-penetration of the contrast agents. The mentioned models are conceptually different, while their mathematical models are the same. In the following section, we will discuss the Meier-Zierler model since we used a non-penetrating contrast agent. Initially, the residue function was defined, as follows [12]:

$$R(t) = 1 - \int_0^t h(\tau) d\tau \quad (1)$$

where h is the vascular transport function. The density time diagram of the tissue was related to the density time diagram based on the following convolution equation:

$$C_T = F \int_{-\infty}^t C_A(t - \tau) R(\tau) d\tau = F(C_A \otimes R) \quad (2)$$

where F is the flow rate (same as cerebral blood flow (CBF)), and CA represents the arterial input function (AIF). Equation 2 was used to control the perfusion measurements. The convolution of the residue function and AIF are required to calculate the flow rate. Cerebral blood volume (CBV) and mean transit time (MTT) are the other parameters that are involved in perfusion, which were calculated based on the following equations [13, 14]:

$$CBV = \frac{\int_{-\infty}^{\infty} C_T dt}{\int_{-\infty}^{\infty} C_A dt} \quad (3)$$

$$MTT = \frac{CBV}{CBF} \quad (4)$$

Design of the capillary network

In the design of the phantom, the tree pattern was used based on the quantitative studies regarding the cardiovascular network and Murray’s minimum work law [15] in order to simulate the hemodynamics of the vessels (Fig 1). According to Murray’s law, nature uses a minimum of four energies, and the relationship between the diameter and bifurcation angle of the capillaries is determined, as follows [16]:

$$\frac{r_0^3}{f_0} = \frac{r_1^3}{f_1} = \frac{r_2^3}{f_2} = const \quad (5)$$

$$\cos(\theta_1) = \frac{r_0^4 + r_1^4 - r_2^4}{r_1^4 r_2^4} \quad (6)$$

$$\cos(\theta_2) = \frac{r_0^4 + r_2^4 - r_1^4}{r_1^4 r_2^4} \quad (7)$$

where $r_0, r_1,$ and r_2 are the radii of the main and daughter channels, θ_1 and θ_2 shows the bifurcation angles, and $f_0, f_1,$ and f_2 represent the flow in the main and daughter channels.

Although Murray’s law is also applicable to circular channel sections, we used rectangular sections due to the prospective difficulties in fabrication[17]. In order to apply Murray’s law to the rectangular sections, the following formula was used in the calculations and designs:

$$\alpha_n (1 + \alpha_n) P_0 (\alpha_n^*) = (2X)^n \alpha_n (1 + \alpha_0) P_0 \alpha_0^* \quad (8)$$

where α_n and α_n^* denote the ratio of the depth (d) to the width (w) of the channel (n) with the depth of less than the width. The capillary network was comprised of two main structural components, including the supplying channels and cells. The supplying channels were relatively large, and Murray’s law could control the bifurcation. The width of the channels with various generations is presented in Table 1.

Table 1. Width of Supplying Microchannel in Theory and in Phantom

Generation	Phantom (μm)	Theory* (μm)
1	5038.345	1085
2	2887.98	597
3	1850.08	353
4	298.011	230
5	71	25

*Calculated using Eq. (8)

Accordingly, the first three generations were not within the four parallel rectangular blocks, while the next four generations were limited

to the blocks. Each block consisted of eight cells, which resembled the capillary beds in the actual microvasculature. The dimensions of the microchannel in each block were approximated based on the findings of Pawlik et al. [18] and Cassot et al. [19](Fig 2).

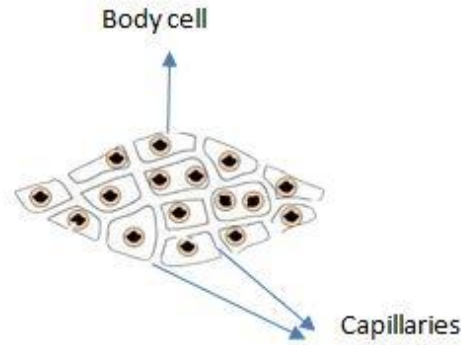


Fig 1. Shape of capillary network inside body

Various calculations of the capillary network were performed based on these theories. Afterwards, the capillary network was designed using the AutoCAD software (M.49.0.0 AutoCAD 2016, Autodesk, Inc., San Rafael, CA, USA) using the parameters obtained from the calculations (Fig 2).

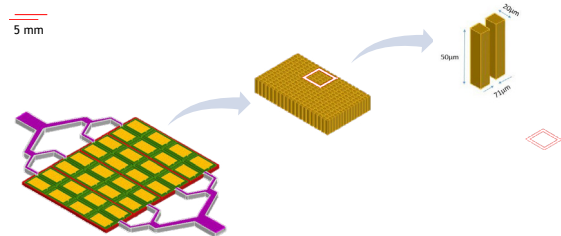


Fig 2. Capillary network geometry (Network contained four parallel blocks (each with eight cells), and each cell contained 100 features separated by channels with width of 71 μm; these features supplied various pathway for blood flow).

Microfabrication

A mold was generated based on the designed network using the soft lithography method. To fabricate the mold, silicon wafer (101.6 mm) with SU-8, 2100 (MicroChem Corp., Boston, MA) was used as the photoresist. The coating (thickness: 240 μm) had the maximum aspect ratio of 1:10. For the coating of the mold, we applied tetrachloro-1,1,2,2-tetrahydrooctyl)-1 trichlorosilane (Sigma-Aldrich Co., USA), also known as silane, by the exposure of the mold through CVD for 45 minutes. This was a critical step since polydimethylsiloxane (PDMS; the silicon-based polymer used at the final

stage for the casting of the material) developed highly potent silicon, which could also function as the silicon bonds to the mold. The prepared mole could be used repeatedly to provide the samples (Fig 3).

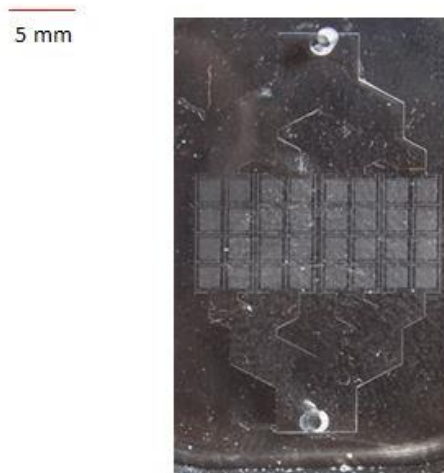


Fig 3. Micro-phantom fabricated using lithographic techniques (two holes on top and bottom of phantom are for injections (entrance) and exit of water or contrast agent; this micro-phantom was used for microfluidic experimental validation)

PDMS was used as the casting material, which is a widely utilized silicon-based polymer. Before use, PDMS should be combined with an activator (10:1). The sample was baked at the temperature of 65°C for three hours prior to removal from the mold. In order to weld the sample to a glass substrate, we employed corona oxygen plasma (Electro-Technic Products Inc.). The treatment of PDMS with the oxygen plasma caused strong PDMS silicon polymerized bonds. In addition, it converted the hydrophobic PDMS into a hydrophilic material temporarily, thereby facilitating the blood flow in the microchannel and minimizing the possibility of air bubble trap in the channels. For approximately 10 minutes, the dry surface remains hydrophilic, and by increasing the time that the surface remains wet, this period could be prolonged.

Experimental setup

Magnevist® (gadopentetate dimeglumine) was injected into the capillary network using a pump attached to the micro-phantom cavity via a connector. Subsequently, the micro-phantom was placed in the middle of the rat coil, and 300 microliters of distilled water was injected each time. A gradient spin echo pulse sequence (TE=5

ms, TR=860 and 1,650 ms after averaging twice) was also employed to collect the images. The selected field of view was 6 cm ×6 cm, and the resolution was 32×32 pixels. The microchannel volume to the total voxel size ratio was equal to the CBV parameter in actual perfusion measurements. The flow rate of the IV pump was 0.00216-0.023 ml/s. For the volume of the network and density of PDMS, these flows yielded 0.2-1.75 ml/100 g/s tissue flow rates.

Simulation

Three-dimensional navier-stokes equations

A simple approach to understanding the 3D description of blood flow is the motion of an incompressible, Newtonian fluid inside a vessel with rigid walls. This description eliminates the interaction of the blood and vessel wall.

Assuming that $\Omega \subset \mathbb{R}^3$ denotes a piece of a blood vessel, the boundary of Ω was decomposed into three subsets, including an upstream cross-sectional area (Γ_{up}), a downstream boundary (Γ_{down}), and the vessel wall (Γ_{wall}) upstream and downstream referring to the main direction of the flow.

To model the hemodynamics, blood was simplified as an incompressible, Newtonian fluid. The latter properties indicated a fluid in which various stresses are linearly proportional to the local strain rate by the viscosity parameter. Evidently, the blood was composed of particles of different nature, generating complicated mechanical properties. However, these effects were only significant when the particle size was relative to the vessel size; in other words, it was proportional to the blood flow in the smallest vessels. The Newtonian approximation remained valid, while the shear strain rate remained above 100 s^{-1} . Therefore, it is mostly used for large- to medium-sized vessels.

Based on the principle of mass and momentum conservation, these assumptions led to the description of the blood flow dynamics based on the following incompressible Navier-Stokes equations:

$$\rho \partial_t v + \rho v \nabla v + \nabla p - 2\eta \nabla \cdot \epsilon(v) = f \quad (9)$$

$$\nabla \cdot v = 0$$

The equations above are comprised of a non-linear, parabolic, partial, differential equation system for velocity ($v: \Omega \times \mathbb{R}^+ \rightarrow \mathbb{R}^3$) and pressure ($p: \Omega \times \mathbb{R}^+ \rightarrow \mathbb{R}$). In equation nine, ρ and η represent

the blood density and viscosity, respectively, and show the strain rate tensor. The term f on the right of equation nine represents the external forces. On the left side, the first two terms indicate inertia, and the other two terms denote the pressure force and viscous force. The system shown in equation nine requires an initial condition, which is provided by a divergence-free velocity field and proper boundary conditions. Moreover, a typical set of boundary conditions [20] should cover the velocity at the upstream boundary and pressure on the downstream boundary, along with a no-slip condition on the vessel wall, as follows:

$$v = v_{up}, \text{ on } \Gamma_{up}$$

$$v = 0_{up}, \text{ on } \Gamma_{wall} \tag{10}$$

$$\varepsilon(v)n - pn = -p_{down}n, \text{ on } \Gamma_{down}$$

where n indicates the normal to the boundary directed outward the fluid domain, and P_{down} denotes the prescribed downstream pressure. In practice, it is better to impose the pressure generated by the response to the blood flow of the truncated distal part of the circulation.

These steps need the close interaction of modelers and clinicians as only in rare cases, measurements are directly applied as boundary conditions. Undeniably, flow rate measurement is possible after selecting a velocity profile, which results in the velocity boundary condition. In the present study, the measurements were not performed where the boundary conditions should be prescribed [21].

Additionally, to facilitate predictions (e.g., surgical planning), it is preferable to impose a correlation between pressure and flow rather than each parameter alone. This results in the coupling of this 3D model with the reduced models, which requires their parameterization using the patient data.

Table 2. Properties of Blood and Gd NPs

Blood properties	Unit	Value
Density	Kg/m ³	1,055
μ	ns/m ²	0.012
n		0.8
Viscosity-Newtonian	ns/m ²	0.0032
Thermal Conductivity	W/mk	0.52
r_p	m	$0.01 - 1 * 10^{-6}$
Specific Heat Capacity	j/kg.k	4200

From mathematical (coupling conditions), numerical (stable and efficient algorithms), and software perspectives (handling of codes possibly by different teams), multi-scale or multi-domain modeling is associated with substantial challenges. Various methods have been proposed to tackle these issues [21] Table 2. shows the properties of blood and Gd NPs.

Microfluidic experimental validation

The results of the simulation were compared with the results of an experimental study on NP distribution, which was conducted using a fabricated micro-phantom similar to the one described in the previous section (NP distribution through a microfluidic channel with the width of 71 μ m).

RESULTS

Flow measurement using MRI in the micro-phantom

Fig 4 shows the contrast agent intensity across the channel in the microfluidic tests. As can be seen, the concentration of the contrast agent was calculated across the channel based on the signal strength of the images.

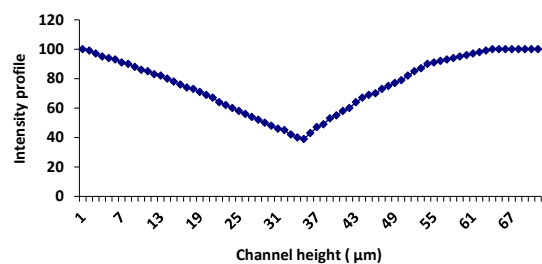


Fig 4. Contrast agent intensity across channel in microfluidic tests practically performed on micro-phantom

Fig 5 depicts the MRI image of the phantom. As is observed, the images obtained from the MRI machine were black and white, while the colored images were rated for the better visualization of the nanomaterials in the micro-phantom.

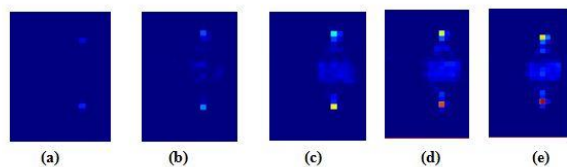


Fig 5. Micro-phantom image obtained by Magnetom 3T Prisma MRI Scanner (Siemens, Munich, Germany); a) Three seconds before injection, b) Three seconds after injection, c) Five seconds after injection, d) 10 seconds after injection, e) 12 seconds after injection.

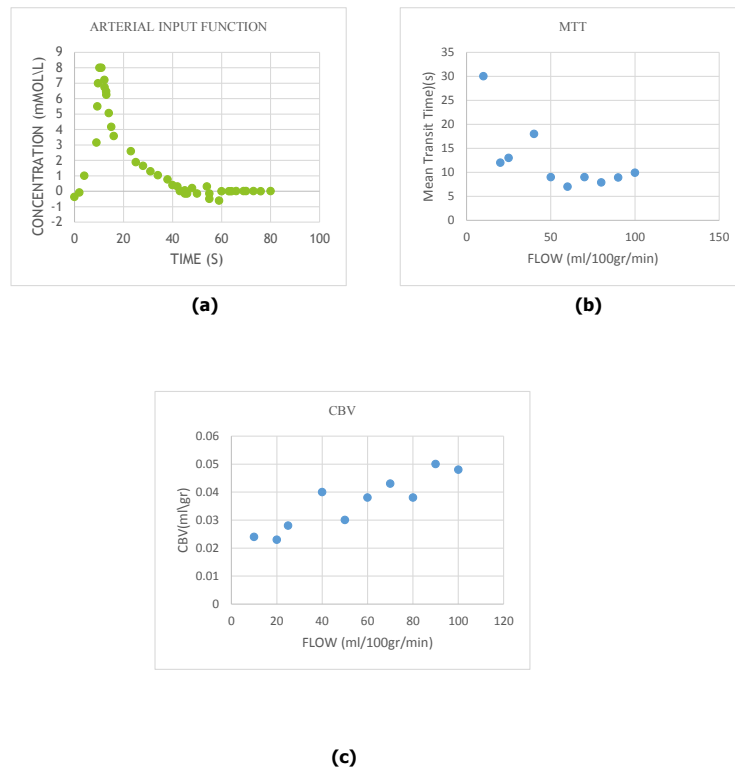


Fig 6. Values of a) AIF, b) CBV, and c) MTT measured in micro-phantom

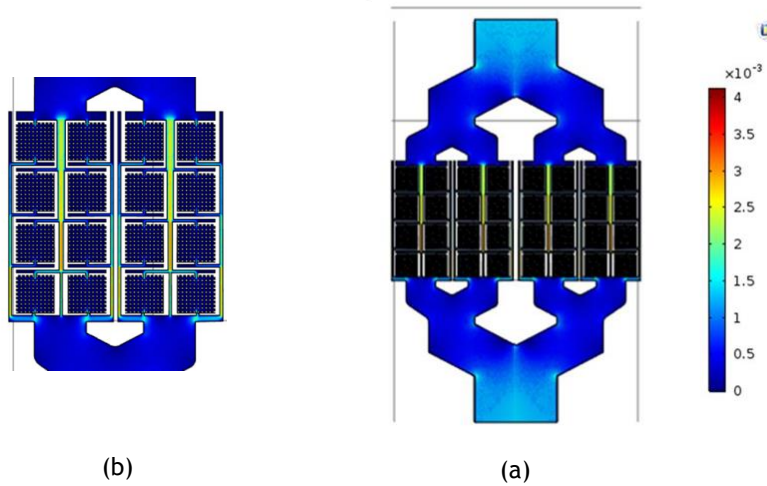


Fig 7. Velocity map of capillary network obtained using COMSOL simulation software version 5.3 (highest velocity observed in capillary network)

Fig 6-a shows a plot of time versus the concentration of the contrast agent. The concentration-time curve was obtained for each pixel in the image. Comparison of Fig 6-a with the standard clinical data of the brain perfusion MRI examination indicated that the perfusion phantom could accurately copy the brain perfusion in terms

of the shape and duration of the concentration-time curve.

Fig 5-c depicts the CBV calculated using equation three. With the CBV and MTT values previously determined, the CBF value could be obtained using equation four. In this regard, the blood flow (CBF) through the system within the

tissue was assumed to be constant.

The units for CBF are often normalized by dividing their absolute values by the mass of the perfused tissue, thereby resulting in the units of the form (ml/min/100 g).

No pooling or blood loss was allowed, so that everything that flows in will eventually flow out.

In the current research, the curves of MTT (Fig 6-b) and CBV (Fig 6-c) were plotted based on the CBF value using equation micro-phantom.

Flow simulation

The velocity map of the capillary network was obtained using the COMSOL simulation software

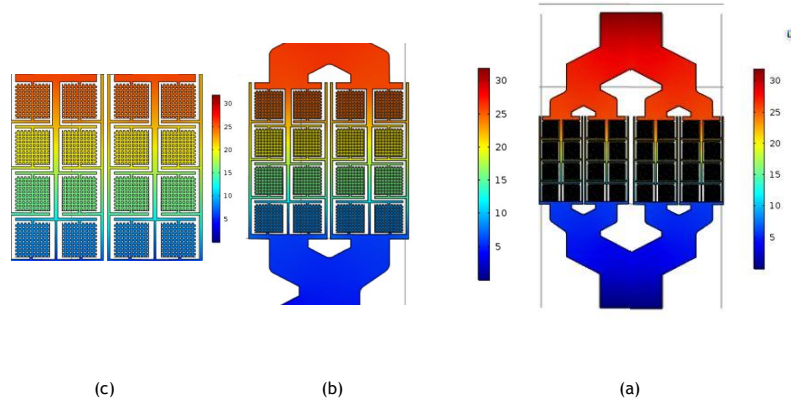


Fig 8. Pressure map of capillary network obtained using COMSOL simulation software version 5.3 (highest pressure (red) on interstitial side of capillary network, which decreased as capillary mesh output was approached (blue))

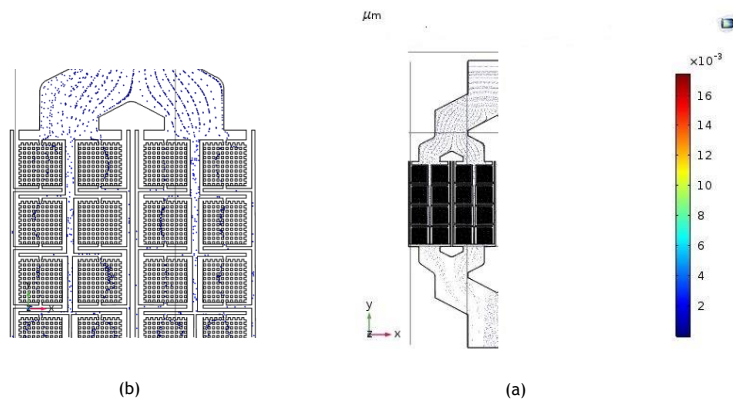


Fig 9. Simulation of Gd distribution and velocity with diameter of 10 nanometer in capillary network

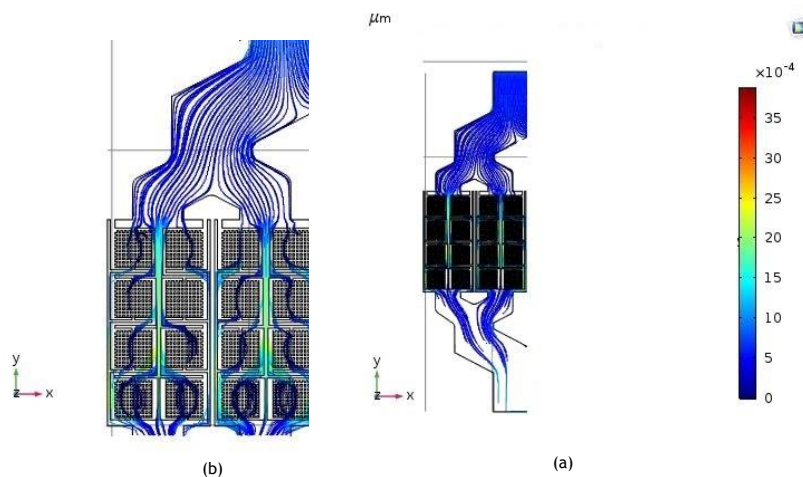


Fig 10. Simulation of Gd distribution and velocity with diameter of 50 nanometers in capillary network

(Fig 6). As can be seen in Fig 6, the velocity in the capillary network was within the range of 0.0001-0.0005 m/s.

The pressure map of the capillary network was also obtained using the COMSOL simulation software (Fig 7).

As is depicted in Fig 7, the highest pressure (red) was on the interstitial side of the capillary network, which decreased as the capillary mesh output was approached (blue). The pressure in the capillary network was within the range of 5-25 mmHg.

Simulations of transport of the NPs

Fig 9 shows the simulation of Gd distribution and velocity with the diameter of 10 nanometer in the capillary network. In order to accelerate the computation with the software, half of the micropathomic simulation was used since the micropathomy was symmetric.

Fig 10 shows the simulation of Gd distribution and velocity with the diameter of 50 nanometers in the capillary network. In order to accelerate the computation with the software, half of the micropathomic simulation was used since the micropathomy was symmetric.

Fig 11 shows the simulation of Gd distribution and velocity with the diameter of one micron in the capillary network. In order to accelerate the computation with the software, half of the micropathomic simulation was used since the micropathomy was symmetric.

the simulated velocity in the capillary network was within the range of 0.0001-0.0005 m/s (Fig 6), which is consistent with the findings of *Ivanov et al* [22].

The simulated pressure in the capillary network was within the range of 5-25 mmHg (Fig 7), which is in line with the findings of *Shore et al.* [23].

Furthermore, the AIF in the phantom was observed to have similar properties to the *in-vivo* equivalent [24].

Based on these findings, the phantom could be used to simulate blood perfusion in tissues and examine the MeierZierler models of perfusion imaging with an MRI scanner.

Based on the mentioned findings, the phantom could also be used to examine the movement of NPs. One of the foremost advantages of the phantom and MRI device was the use of a perfusion imaging protocol.

AIF is a key parameter in this protocol, which is based on the concentration (mMOL/l) (Fig 6-a), so that in each branch of the microphantom, the approximate concentration of the concentration of the contrast agent (NPs) could be calculated.

As is depicted in Fig 6-b, the other parameter was MTT, which could be used to calculate the average transit time of the nanomaterials in each region of the micro-phantom.

According to Fig 6-b, another parameter in this regard was CBV, which was used to calculate the average transit time of the nanomaterials in each region of the micro-phantom. These parameters were measured in the capillary input area using the

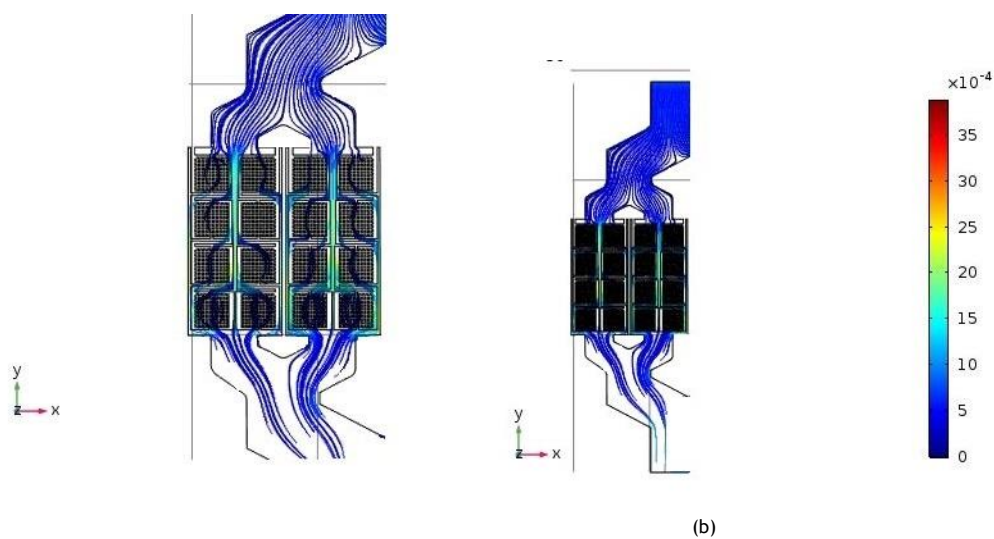


Fig 11. Simulation of Gd distribution and velocity with diameter of one micron in capillary network

MRI device. According to Fig 1, the concentration of the nanomaterials upon entry into the capillary network was significant, while the concentration decreased over time.

As is shown in Fig 4, comparison of the core region indicated that the MRI NP intensity increased, becoming close to the channel wall, which is consistent with the simulated NP distribution profile depicted Figs 9-11. However, after the removal of the NPs from the capillary network, the movement of the NPs was observed to be lower on the sides of the vessel.

According to Fig 5, the maximum concentrations of the contrast agent were inside the capillary network, and only 25% of the NPs entering the capillary network were removed from the network. This is consistent with the simulation results shown in Figs 9-11. According to Figs 9-11, the velocity of the NPs in the region with the maximum velocity and pressure blood flow was highest. Furthermore, the pattern of NP movement was found to be the same. After the removal of the NPs from the capillary network, the movement of the NPs decreased at the sides of the vessel, and only 25% of the NPs entering the capillary network were removed from the network.

ACKNOWLEDGMENTS

This article was extracted from a thesis funded by Tehran University of Medical Sciences (TUMS), Iran (grant number: 9413338003). Hereby, we extend our gratitude to TUMS for the financial support of this study. We would also like to thank the staff of the University of Sharif Microelectronics Laboratory and the National Brain Mapping Laboratory (NBML) for hosting the fabrication process of this research and providing the technical support, guidance, and access, as well as Amir Kabir Cloud Computing Portal (HPCRC) for the simulation, which was performed under contract number ISI-DCE-DOD-Cloud-700101-1990 at Amir Kabir University in Tehran, Iran.

REFERENCES

1. Wang T, Yang S, Petrenko VA, Torchilin VP. Cytoplasmic delivery of liposomes into MCF-7 breast cancer cells mediated by cell-specific phage fusion coat protein. *Mol Pharm.* 2010; 7(4): 1149-1158.
2. Al-Jamal WT, Kostarelos K. Liposomes: from a clinically established drug delivery system to a nanoparticle platform for theranostic nanomedicine. *Acc Chem Res.* 2011;44(10):1094-1104.
3. Choudhury RP, Fuster V, Fayad ZA. Molecular, cellular and functional imaging of atherothrombosis. *Nat Rev Drug Discov* 2004;3(11): 913.
4. Gao X, Yang L, Petros JA, Marshall FF, Simons JW, Nie S. In vivo molecular and cellular imaging with quantum dots. *Curr Opin Biotechnol* 2005; 16(1): 63-72.
5. Roy I, Ohulchanskyy TY, Pudavar HE, Bergey EJ, Oseroff AR, Morgan J, et al. Ceramic-based nanoparticles entrapping water-insoluble photosensitizing anticancer drugs: A novel drug-carrier system for photodynamic therapy. *J Am Chem Soc.* 2003;125(26): 7860-7865.
6. Huang X, El-Sayed IH, Qian W, El-Sayed MA. Cancer cell imaging and photothermal therapy in the near-infrared region by using gold nanorods. *J Am Chem Soc.* 2006;128(6): 2115-2120.
7. Sardar R, Shumaker-Parry JS. Asymmetrically functionalized gold nanoparticles organized in one-dimensional chains. *Nanoscale Res Lett* 2008; 8(2): 731-736.
8. Park JH, von Maltzahn G, Zhang L, Derfus AM, Simberg D, Harris TJ, et al. Systematic surface engineering of magnetic nanoworms for in vivo tumor targeting. *small.* 2009;5(6): 694-700.
9. Dai Q, Worden JG, Trullinger J, Huo Q. A "nanonecklace" synthesized from monofunctionalized gold nanoparticles. *Journal of the American Chemical Society.* 2005; 127(22) :8008-8009.
10. Decuzzi P, Ferrari M. The adhesive strength of non-spherical particles mediated by specific interactions. *Biomaterials.* 2006; 27(30): 5307-5314.
11. Kety SS, Schmidt CF. The determination of cerebral blood flow in man by the use of nitrous oxide in low concentrations. *Am J Physiol* 1945;143(1): 53-66.
12. Meier P, Zierler KL. On the theory of the indicator-dilution method for measurement of blood flow and volume. *J Appl Physiol* 1954 ;6(12): 731-744.
13. Shurche S, Alam NR. Simulation of Capillary Hemodynamics and Comparison with Experimental Results of Microphantom Perfusion Weighted Imaging. *J Biomed Phys Eng* 2019.
14. Mehta A, Jones BP. *Neurovascular Diseases.* Grainger & Allison's Diagnostic Radiology: Neuroimaging. 2015: 68.
15. Murray CD. The physiological principle of minimum work: I. The vascular system and the cost of blood volume. *Proc Natl Acad Sci U S A* 1926; 12(3): 207.
16. Rossitti S, Löfgren J. Vascular dimensions of the cerebral arteries follow the principle of minimum work. *Stroke.* 1993; 24(3): 371-377.
17. Emerson DR, Cieřlicki K, Gu X, Barber RW. Biomimetic design of microfluidic manifolds based on a generalised Murray's law. *Lab Chip.* 2006; 6(3): 447-454.
18. Pawlik G, Rackl A, Bing RJ. Quantitative capillary topography and blood flow in the cerebral cortex of cats: an in vivo microscopic study. *Brain Res.* 1981; 208(1): 35-58.
19. Cassot F, Lauwers F, Fouard C, Prohaska S, LAUWERS-CANCES V. A novel three-dimensional computer-assisted method for a quantitative study of microvascular networks of the human cerebral cortex. *Microcirculation.* 2006; 13(1): 1-18.
20. Vignon-Clementel IE, Figueroa CA, Jansen KE, Taylor CA. Outflow boundary conditions for three-dimensional finite element modeling of blood flow and pressure in arteries. *Comput Methods Appl Mech Eng.* 2006; 195(29-32): 3776-3796.
21. Arbia G, Corsini C, Moghadam ME, Marsden AL,

- Migliavacca F, Pennati G, et al. Numerical blood flow simulation in surgical corrections: what do we need for an accurate analysis? *JAMA Surg.* 2014; 186(1): 44-55.
22. Ivanov K, Kalinina M, Levkovich YI. Blood flow velocity in capillaries of brain and muscles and its physiological significance. *Microvasc Res* 1981; 22(2): 143-155.
23. Shore AC. Capillaroscopy and the measurement of capillary pressure. *Br J Clin Pharmacol* 2000; 50(6): 501-513.
24. Calamante F, Mørup M, Hansen LK. Defining a local arterial input function for perfusion MRI using independent component analysis. *Magn Reson Med.* 2004; 52(4): 789-797.